Check for updates

RESEARCH ARTICLE

Lithium-Sulfur Batteries

Energy & Environmental Materials WILEY

Electrochemical Realization of 3D Interconnected MoS_3/PPy Nanowire Frameworks as Sulfur-Equivalent Cathode Materials for Li-S Batteries

*Hongtao Yu, Andreas Siebert, Shilin Mei, Raul Garcia-Diez, Roberto Félix, Ting Quan, Yaolin Xu, Johannes Frisch, Regan G. Wilks, Marcus Bär, Chun Pei, and Yan Lu**

The development of freestanding and binder-free electrode is an effective approach to perform the inherent capacity of active materials and promote the mechanism study by minimizing the interference from additives. Herein, we construct a freestanding cathode composed of MoS_3/PPy nanowires (NWs) deposited on porous nickel foam (NF) (MoS_3/PPy/NF) through electrochemical methods, which can work efficiently as sulfur-equivalent cathode material for Li-S batteries. The structural stability of the MoS_3/PPy/NF cathode is greatly enhanced due to its significant tolerance to the volume expansion of MoS_3 during the lithiation process, which we ascribe to the flexible 3D framework of PPy NWs, leading to superior cycling performance compared to the bulk-MoS_3/NF reference. Eliminating the interference of binder and carbon additives, the evolution of the chemical and electronic structure of Mo and S species during the discharge/charge was studied by X-ray absorption near-edge spectroscopy (XANES). The formation of lithium polysulfides was excluded as the driving cathode reaction mechanism, suggesting the great potential of MoS_3 as a promising sulfur-equivalent cathode material to evade the shuttle effect for Li-S batteries. The present study successfully demonstrates the importance of structural design of freestanding electrode enhancing the cycling performances and revealing the corresponding mechanisms.

1. Introduction

Lithium-sulfur (Li-S) batteries have attracted ample attention due to their high theoretical capacity (~1675 mAh g^{-1}), as well as the cheap and environmentally friendly properties of sulfur used as active material in the cathode.[1–5] However, the "shuttle effect" of lithium polysulfides during cycling,[3,6] the insulating nature of sulfur and its full discharge products (Li_2S, Li_2S_2),[7,8] together with the large volume expansion resulting from the insertion of Li^+, so far still limit the stability of the battery performance.[9] The insulating nature of sulfur and lithium sulfides is mainly responsible for the low utilization of sulfur. Therefore, electric conductors (e.g. the widely used carbon additives) are necessary to construct a conducting network in the cathode. Good conductivity as high as that of carbon materials (i.e. 0.1 to 10^2 S cm^{-1})[10] has been mostly pursued in Li-S cathode to facilitate the redox reaction of sulfur species. Besides, the main problem arises from the dissolution of the reaction intermediates in the organic electrolyte causes the loss of active sulfur and fast decay of specific capacity during charge–discharge processes. To tackle these issues, research efforts are ongoing to develop cathode materials with a more porous structure and high conductivity. In most cases, various functional materials (e.g. carbonaceous materials, metal oxides and sulfides, and polymers) pose a modest ability in the cathode to diminish the dissolution of polysulfides in the electrolyte through the physical and chemical confinement strategies.[11–18] For the physical confinement, the formed polysulfides can be entrapped in the porous and hollow structures of the cathodes, which can provide weak adsorption and physical barrier to suppress the diffusion of polysulfides into electrolyte. As for the chemical confinement, polar surface of host materials such as metal oxides/sulfides/nitrides can provide strong chemical adsorption to

Dr. H. Yu, Dr. S. Mei, Dr. T. Quan, Dr. Y. Xu, Prof. Y. Lu
Department for Electrochemical Energy Storage, Helmholtz-Zentrum Berlin für Materialien und Energie GmbH (HZB), Hahn-Meitner Platz 1, 14109 Berlin, Germany
E-mail: yan.lu@helmholtz-berlin.de
Dr. H. Yu, Dr. C. Pei
Guangdong Province Key Laboratory of Durability for Marine Civil Engineering, School of Civil Engineering, Shenzhen University, Shenzhen, Guangdong 518060, China
Dr. A. Siebert, Dr. R. Garcia-Diez, Dr. R. Félix, Dr. J. Frisch, Dr. R. G. Wilks, Prof. M. Bär
Department of Interface Design, HZB, Albert-Einstein-Str. 15, 12489 Berlin, Germany
Dr. R. G. Wilks, Prof. M. Bär
Energy Materials In-Situ Laboratory Berlin (EMIL), Albert-Einstein-Str. 15, 12489 Berlin, Germany
Prof. M. Bär
Helmholtz-Institute Erlangen-Nürnberg for Renewable Energy (HI ERN), Albert-Einstein-Str. 15, 12489 Berlin, Germany
Prof. M. Bär
Department of Chemistry and Pharmacy, Friedrich-Alexander-Universität Erlangen-Nürnberg, Egerlandstr. 3 91058, Erlangen Germany
Prof. Y. Lu
Institute of Chemistry, University of Potsdam, 14467, Potsdam Germany
The ORCID identification number(s) for the author(s) of this article can be found under https://doi.org/10.1002/eem2.12539.

DOI: 10.1002/eem2.12539

© 2022 The Authors. *Energy & Environmental Materials* published by John Wiley & Sons Australia, Ltd on behalf of Zhengzhou University. This is an open access article under the terms of the Creative Commons Attribution License, which permits use, distribution and reproduction in any medium, provided the original work is properly cited.

polysulfides. Additionally, covalent binding formed between organic host materials and sulfur species can efficiently alleviate the "shuttle effect" of polysulfides. For instance, hollow carbon nanofibers have been fabricated for the physical confinement of polysulfides;[16] the conducting polymer with the thiol groups has been designed and synthesized for the chemical confinement of polysulfides;[19] furthermore, the metal–organic framework derived NiS_2 hollow spheres can prevent the migration of polysulfides through the combined physical and chemical adsorption.[17]

The application of sulfur-equivalent cathode materials shows great potential to solve the shuttle problem completely due to its distinct reaction mechanism, where soluble polysulfides are unlikely to form during the discharge process, different from that of elemental sulfur. Thus, alternatives to elemental sulfur, including organic[20] and inorganic sulfides[21] that do not form soluble polysulfides during the discharge process, are considered more feasible for Li-S battery applications. Although organic sulfides have been studied extensively for decades, their low theoretical capacity (LiS-R and Li_2S as the final discharge products) an low conductivity (e.g. 10^{-10} S cm^{-1} for Poly (5,8-dihydro-1H,4H-2,3,6,7-trtrathia-anthracene) (PDTTA))[22] make them impractical for Li-S batteries.[2,6,23–25] Inorganic polysulfides (Li_2S as the final discharge products) have electrochemical properties comparable to elemental sulfur, significantly higher conductivity (e.g. 10^{-3} S cm^{-1} for MoS_3, while 10^{-30} S cm^{-1} for S) and are believed not to generate lithium polysulfides—however, this has not been experimentally verified.[26] As one of the inorganic sulfides used as sulfur-equivalent cathode materials, MoS_3 without containing of elemental sulfur has a significantly high conductivity and can exhibit sulfur-like electrochemical behaviors. Moreover, MoS_3 has facile fabrication process including the acidification or anodic oxidation of aqueous solutions of $(NH_4)_2MoS_4$ at room temperature.[3,21] Despite its great potential, the underlying lithiation mechanism has rarely been investigated. Recently, it was reported that no polysulfides are formed and no Mo-S bonds break during discharge/charge.[21] However, a reaction mechanism has not been conclusively agreed upon, due to the complex chemistry involved. In this regard, developing a free-standing, binder- and carbon additive-free, and porous cathode with flexible polymeric nano-host for metal sulfides is not only favorable to achieving high specific capacities and stable cycling performances but also helpful for detailed characterization such as ex situ analysis on morphological and compositional evolution of the active materials without interference from the conventional binder and carbon additive. Additional advantages of such free-standing electrodes would be the ease of collection and analysis after the disassembly of the batteries.

Advances in exploiting nanoarchitecture of electrochemically active materials on the conducting substrate open up new directions to address the limitations of compact and bulk electrode materials in terms of high electrolyte penetration for effective Faradaic reactions and their functionalization for flexible electronic devices. Among tremendous efforts, electropolymerization/electrodeposition, as a practical method for the synthesis of conducting polymers (CPs) on conductive substrates, shows great potential for the construction of the aforementioned electrode materials. On one hand, conducting polymers can serve as a template for in situ growth of inorganic active materials due to their ease of functionalization, which enables a high active mass loading in the batteries. On the other hand, a continuous conducting framework can be preserved after the active material loading. Particularly, nanostructured conducting polymers usually assure quick diffusion of electrolytes due to their large surface area and porous structure, which can also relieve the volume expansion during the lithiation process.[27] As one common CP, polypyrrole (PPy) has often been used in the development of functional electrode materials, notably due to its environmental stability and high electronic conductivity.[28] Owing to nanotechnological advances, the deliberate design of CP's nanoarchitecture is feasible for further improving its electrical and ionic conductivity. So far, the PPy nanowire (NW) structure has been fabricated, exhibiting electrochemical performance superior to other structural forms of PPy,[29,30] posing a great potential for its adoption in Li-S batteries. According to previous studies, the electrochemical growth of PPy NWs using the soft-template method is of great interest because of its facile and controllable characteristics for large-area fabrication.[31,32] Generally, a noble metal (e.g. Au, Pt, and Pd) is needed as the nucleation sites for the electrochemical growth of PPy NWs on substrates.[33–35] Also, carbon materials can assist the formation of nucleation sites for PPy through the strong interactions between pyrrole molecules and carbon substrates. However, there are few reports about the electropolymerization of PPy NWs on non-noble metal substrates such as commercial nickel foam (NF) due to the lack of nucleation sites. Three-dimensional NF is commonly used as the current collector, because it has proven to show excellent electrochemical performance, owing to the large electrode–electrolyte interfaces as well as the macropores of NF, which may act as a reservoir for electrolytes and thus shorten the ion diffusion distance from the exterior to the interior surfaces. Besides, the flexibility and high electrical conductivity make NF ideal current collectors for flexible electrode materials.[36]

Inspired by these developments, we propose to realize the direct electrochemical growth of PPy NWs on NF, which can be further used as a template to fabricate MoS_3/PPy composite NWs as free-standing cathode materials for Li-S batteries.

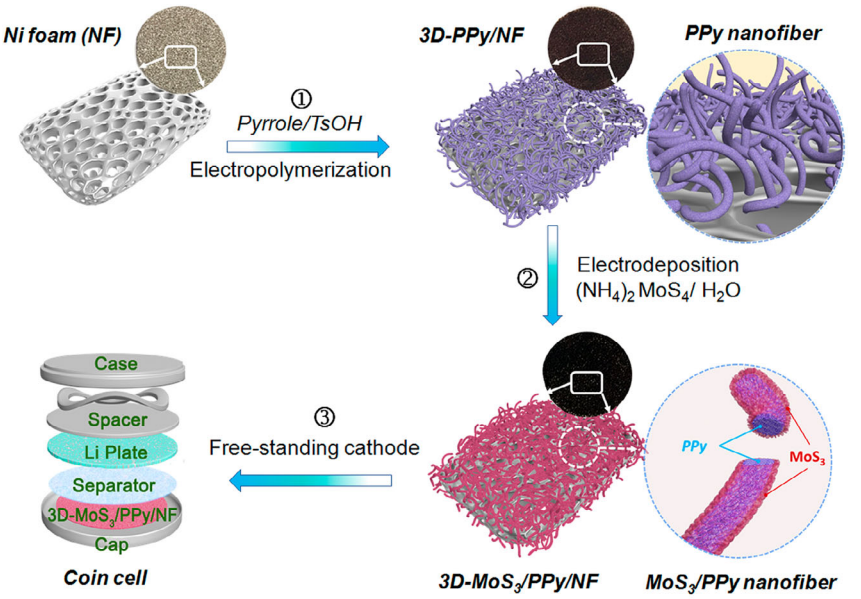
2. Results and Discussion

2.1. Structure and Morphology

As a result of these efforts, a free-standing MoS_3/PPy/NF cathode has been fabricated through facile electrochemical methods (**Scheme 1**), which can be directly used as the sulfur-equivalent cathode. Firstly, through controlling the concentration ratio of pyrrole and soft-template molecule (0.1 M *p*-toluenesulfonic acid; TsOH), PPy NWs with a 3D-network structure were successfully grown on the surface of NF without the assistance of noble metals or carbon materials. Amorphous MoS_3 nanoparticles (NPs) were then coated on the PPy NWs through anodic electrodeposition in the aqueous solution of $(NH_4)_2MoS_4$. Notably, the loading mass of MoS_3 can be conveniently tuned by controlling electrodeposition conditions (e.g. applied voltage, deposition time). With the synergistic effect of flexible PPy NWs and MoS_3 NPs, the 3D-MoS_3/PPy/NF cathode is expected to show a higher capacity and enhanced cycle stability than that of the bulk-MoS_3/NF without PPy NWs. Moreover, identifying or excluding the possible formation of lithium (poly)sulfides is essential to understanding the working mechanism of MoS_3 as cathode materials in Li-S batteries and to developing long-cycle-life devices. A series of bulk-sensitive X-ray absorption near-edge spectroscopy (XANES) measurements have been performed for the MoS_3/PPy/NF cathodes at different stages of discharge/charge to investigate the evolution of the chemical and electronic structure,

© 2022 The Authors. *Energy & Environmental Materials* published by John Wiley & Sons Australia, Ltd on behalf of Zhengzhou University.

25750356, 2024, 2, Downloaded from https://onlinelibrary.wiley.com/doi/10.1002/eem2.12539 by Helmholtz-Zentrum Berlin Für, Wiley Online Library on [12/04/2024]. See the Terms and Conditions (https://onlinelibrary.wiley.com/terms-and-conditions) on Wiley Online Library for rules of use; OA articles are governed by the applicable Creative Commons License



Scheme 1. Fabrication route of the sulfur-equivalent MoS_3/PPy/NF cathode through electrochemical methods.

aiming to unveil the reaction mechanism of MoS_3 during battery cycling.

Scheme 1 describes the fabrication process of sulfur-equivalent MoS_3/PPy/NF cathodes for Li-S batteries. PPy NWs with a 3D-network structure were first fabricated directly on NF through the electropolymerization method as shown in step 1. Typically, the growth of 3D-PPy NWs can be described by four steps: First, the pyrrole molecules are oxidized and oligomers are formed near the surface of NF under positive potential. Second, the electrodeposition of PPy, accompanied by the oxidation of water, leads to the formation of a thin and rough PPy film on NF. Third, the hydroxyl radicals formed during the oxidation of water can either lead to the overoxidation of PPy to prevent its further growth or transform into O_2. The active place of film taken by O_2 nanobubbles can supply growing sites, leading to the formation of PPy NWs in the place of O_2 evolution or flaws.[32] Presumably, this part of polymer survives over-oxidation,[37] and the highest electric field originated from the edge effects leads to the subsequent growth of PPy NWs. Finally, PPy NWs grow through hydrogen bonding and electrostatic attraction between pyrrole oligomers and electrolyte ions with the help of soft-template ions. During the growth of PPy NWs, the color of NF changed gradually from silver to dark brown as shown in Figure S1, Supporting Information. Step 2 in Scheme 1 shows the process of in-situ growth of amorphous MoS_3 NPs on the PPy NWs through anodic electrodeposition, leading to a 3D-MoS_3/PPy/NF cathode. These MoS_3 NPs are then used as the sulfur-equivalent material in the cathode of Li-S batteries. It is notable that this electrochemical fabrication strategy is more convenient than the conventional process of electrode fabrication[38] because no addition of carbon and binder is required.

Figure 1 presents the detailed electrochemical growth process of 3D PPy NWs on NF through a one-step electro-polymerization method without any seed coating. SEM images taken for the samples at various growth stages are shown in Figure 1a. The pyrrole was oxidized and polymerized at a constant current density of 2.0 mA cm^{-2} in a phosphate buffer solution (pH = 6.86). TsOH (0.1 M) was used as the soft template, of which Ts^+ ions can dope in the initially formed PPy oligomers to promote the following forming and growth of PPy NWs at the tips of nuclei.[29] According to previous work, high concentrations of TsOH (higher than 0.08 M) will prevent the formation of PPy NWs during pyrrole polymerization.[29] Thus, a lower concentration of TsOH (0.01 ~ 0.02 M) is normally used to conduct the electrochemically grown PPy NWs on the surface of noble-metal or carbon materials.[33,34] In our case, however, the high concentration of TsOH (0.10 M) is essential to realize the electrochemical growth of PPy NWs on NF. The relevant mechanism will be discussed later. The chronopotentiometric curve for the growing of 3D-network PPy NWs (Figure 1a) can be divided into four phases corresponding to the oxidation of pyrrole (I), the formation of PPy film (II), the forming of PPy short sticks (III), and the following growth of PPy NWs (IV). SEM images of these phases are presented in Figure 1b–e. In the first phase, a smooth surface of bare NF can be observed as shown in Figure 1b. During phase II, a rough PPy film was found uniformly grown on the surface as shown in Figure 1c. Similar to the growing process of PPy NWs on the noble-metal and carbon substrates, the TsOH prevents the random polymer growth of PPy through the doping of TsOH anions in the initially formed PPy oligomers,[29] which leads to the formation of a thin PPy film on the surface of NF in the initial stage of the electropolymerization. Presumably, the π-π interaction between the aromatic rings of TsOH and pyrrole in PPy oligomers and their electrostatic adsorption should be responsible for the morphological control of the electrochemical deposition products of pyrrole. During the prolongation of the polymerization time, the PPy film becomes rougher and with an increasing number of short sticks growing out from the PPy film (phase III), as shown in Figure 1d. At the same time, some ring- and branch-like structures can also be observed, leading to the formation of a 3D network structure of PPy NWs during phase IV (Figure 1e). The TEM image of the obtained PPy NWs in Figure 1e displays a branch structure with a NW diameter of about 110 nm (Figure S2, Supporting Information). After the electropolymerization of pyrrole, the NF was uniformly coated with PPy NWs (Figure 1f). The cross-sectional view of PPy NWs shows the thickness of the initially grown PPy film is about 100 nm, and the PPy NWs layer is about 2 μm (inset of Figure 1f).

To investigate the influence of the pyrrole concentration on the growth of PPy NWs, the electropolymerization process was conducted in a solution containing 0.1 M TsOH and different concentrations of pyrrole (0.058 M, 0.086 M, and 0.115 M). The corresponding morphology of the polymerized PPy is shown in Figure S3, Supporting Information. Notably, at a low concentration of pyrrole (0.058 M), the modified NF has a high density of PPy NWs with a diameter of ~90 nm (Figure S3a,d, Supporting Information). As the concentration of pyrrole was increased to 0.086 M, the amount of the obtained PPy NWs decreases and their diameter increases (Figure S3b,e, Supporting Information). Nickel oxide possesses a certain catalytic ability for oxygen evolution reaction (OER).[39,40] When a positive potential is

© 2022 The Authors. *Energy & Environmental Materials* published by John Wiley & Sons Australia, Ltd on behalf of Zhengzhou University.

25750356, 2024, 2, Downloaded from https://onlinelibrary.wiley.com/doi/10.1002/eem2.12539 by Helmholtz-Zentrum Berlin Für, Wiley Online Library on [12/04/2024]. See the Terms and Conditions (https://onlinelibrary.wiley.com/terms-and-conditions) on Wiley Online Library for rules of use; OA articles are governed by the applicable Creative Commons License

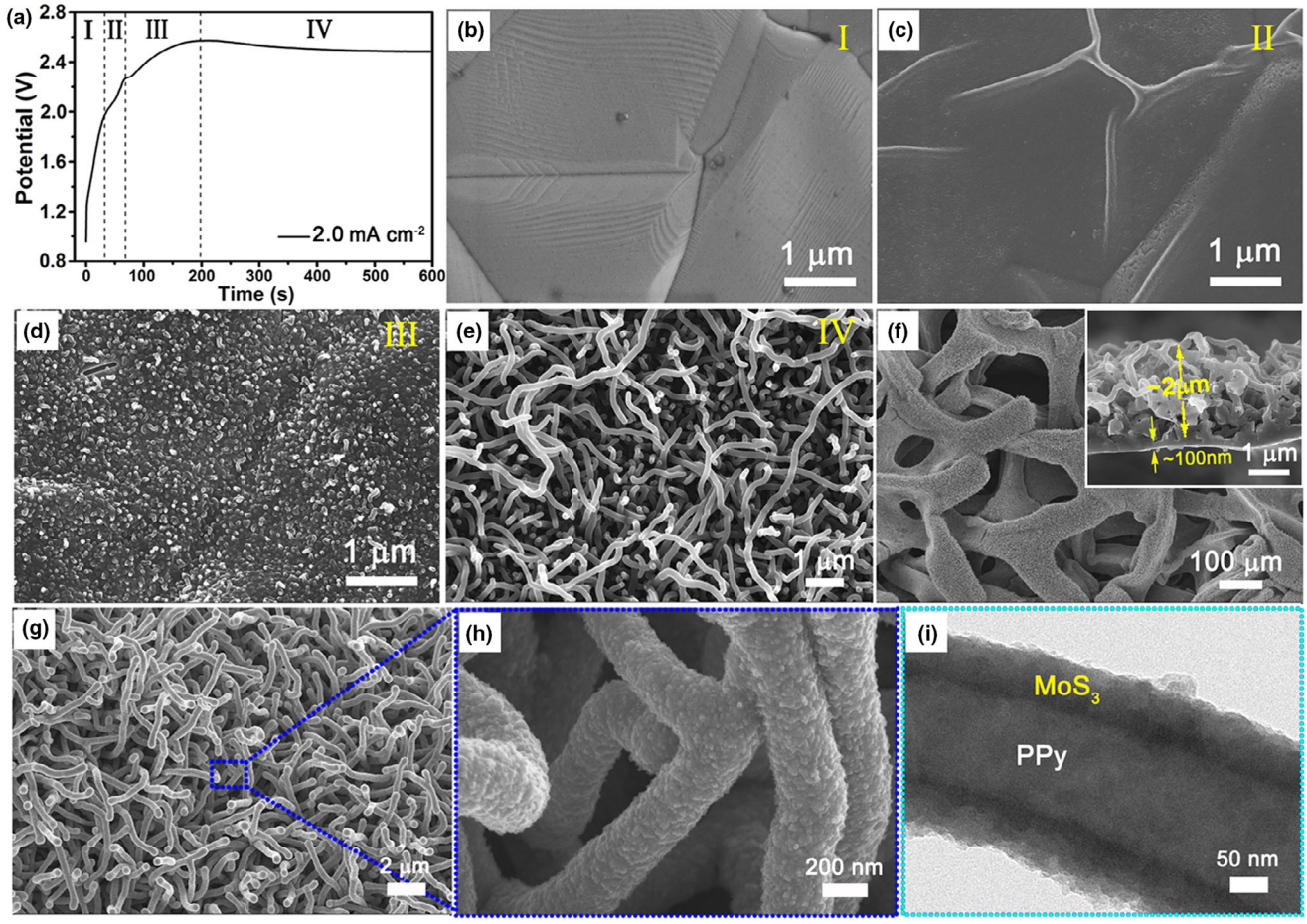


Figure 1. The electrochemical growth process of 3D-PPy NWs on NF: a) chronopotentiometric curve during pyrrole polymerization at 2.0 mA cm^{-2}, including four electrochemical regimes (I, II, III, and IV) corresponding to the growth process of nanowires; SEM images of these processes: b) the surface of NF (I), c) the thin and rough PPy film on NF (II), d) the PPy short sticks on the film (III) and e) the following growth of 3D-PPy NWs (IV); f) PPy/NF electrode with a low magnification (Inset of (f) is the cross-sectional view of PPy NWs). g, h) SEM images of MoS_3/PPy NWs with a low and high magnification; i) TEM image of a single PPy NW coated with MoS_3.

applied, the nickel oxide formed at the NF surface will enhance the OER rate. It is worth noting that plenty of O_2 bubbles will continuously form on the surface of NF at the same applied voltage in the solution without pyrrole. Thus, during the formation of a PPy film under a high concentration of soft-template molecules, the O_2 nanobubbles serve as the growing sites for nanowires.[32] Increasing the concentration of pyrrole inhibits the OER, resulting in a decrease in the growing sites. This effect is evident from the morphology of the electropolymerized PPy at a higher concentration of pyrrole (0.115 M), where few PPy NWs besides bulk PPy films are obtained (Figure S3c,f, Supporting Information). These results indicate that excess TsOH and the catalytic oxidation of water are the key points to realizing the electrochemically grown PPy NWs on the surface of NF. As a result, an optimized condition of 0.1 M TsOH and 0.086 M pyrrole has been applied for the construction of the electrode.

To obtain MoS_3/PPy NW composite samples, MoS_3 NPs were electrodeposited on the surface of 3D-PPy NWs through the oxidation of $(NH_4)_2MoS_4$ by applying a constant positive voltage. To remove the excess MoS_4^{2-} ions adsorbed during anodic electrodeposition and to increase the structural stability of the porous MoS_3, the electrodes were subsequently treated by acidification and annealing at 200 °C. The I-t curves under different applied voltages are shown in Figure S4, Supporting Information. These curves display the classical behavior of nucleation and growth of three-dimensional centers.[40] From the SEM images (Figure 1g,h), we can see that the surface of PPy NWs is coated by MoS_3 NPs with sizes of 20 ~ 50 nm (Figure S5, Supporting Information). TEM images further show that the PPy NWs are uniformly coated with MoS_3 NPs with a thickness of about 50 nm (Figure 1i). More importantly, the loading mass of MoS_3 could be adjusted by tuning the deposition time or voltage (inset of Figure S4, Supporting Information). As shown in Figure S6, Supporting Information, the layer of MoS_3 gradually becomes thicker as increasing the loading mass of MoS_3. These results suggest that the MoS_3 NPs could be electrodeposited on the surface of PPy NWs in situ through the oxidation of $(NH_4)_2MoS_4$ in an aqueous solution, which supplies a simple method for the construction of 3D-MoS_3/PPy composite framework on the conductive substrate. For comparison, MoS_3 has been electrodeposited under the same conditions on NF without PPy NWs. The corresponding SEM images of the MoS_3/NF are displayed in Figure S7, Supporting Information, which reveal

© 2022 The Authors. *Energy & Environmental Materials* published by John Wiley & Sons Australia, Ltd on behalf of Zhengzhou University.

25750356, 2024, 2, Downloaded from https://onlinelibrary.wiley.com/doi/10.1002/eem2.12539 by Helmholtz-Zentrum Berlin Für, Wiley Online Library on [12/04/2024]. See the Terms and Conditions (https://onlinelibrary.wiley.com/terms-and-conditions) on Wiley Online Library for rules of use; OA articles are governed by the applicable Creative Commons License

that MoS_3 is homogeneously coated onto the surface of NF and there is a uniform element distribution of Mo and S (the atomic ratio of S/Mo is ~3).

2.2. Characterization and Electronic Structure

To confirm the amorphous nature of the electrodeposited MoS_3 NPs, the MoS_3/PPy/NF sample was first examined by X-ray diffraction (XRD), which shows a broad peak centered at ~14° besides the sharp peaks (at 45°, 52° and 77°) belonging to the nickel foam (**Figure 2a**). The broad peak is in a good agreement with reported XRD data of amorphous MoS_3.[41] The chemical states of Mo and S in the near-surface region of the sample were further identified by X-ray photoelectron spectroscopy (XPS, see Appendix S1 in supporting information for more details and data evaluation). The fit of the S 2p spectrum presented in Figure 2b indicates the presence of four different species with S $2p_{3/2}$ peaks centered at 162.1, 163.3, 166.2, and 168.6 eV. The higher-binding energy peaks at 166.2 and 168.6 eV correspond to sulfur with an oxidation state of 4+ and 6+, which can be assigned to small contributions of sulfite and sulfate species, respectively.[42] The two peaks at 162.1 eV and 163.3 eV in the S $2p_{3/2}$ spectra relate most likely to S^{2-} and to S^{1-}, respectively, similar to what has been observed for MoS_3 in literature.[42–44] Consequently, the Mo 3d/S 2s spectrum was also fitted using these sulfur species, together with two Mo species as presented in Figure 2c. The Mo $3d_{5/2}$ main peak at 229.4 eV can be related to the Mo^{4+} species of MoS_3 in good agreement with literature values of (229.0 ± 0.2) eV.[43] The small Mo $3d_{5/2}$ peak at 232.4 eV has been assigned to Mo^{6+}, that is MoO_3 (232.1–233.6 eV in literature),[45–47] tentatively ascribed to surface oxidation.

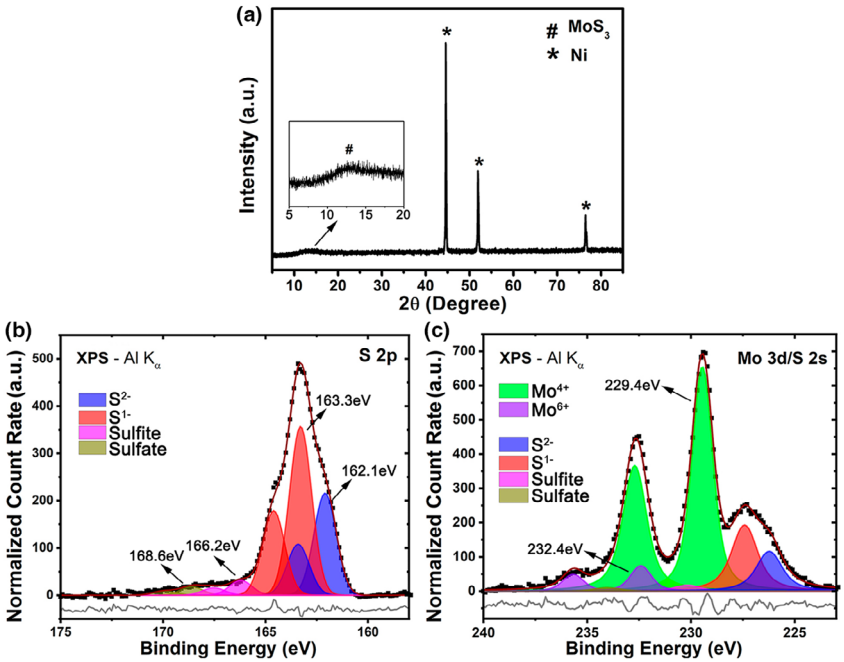


Figure 2. a) X-ray diffraction data, b) S 2p XPS spectrum, and c) Mo 3d / S 2s XPS spectrum of the 3D-MoS_3/PPy/NF.

The concentration of the Mo and S species in the 3D-MoS_3/PPy/NF sample has been determined by taking the average values of the S 2p and S 2s corrected areas, as summarized in Tables S1 and S2, Supporting Information. The sulfite and sulfate species each contribute less than 6% to the total amount of sulfur and Mo^{6+} (MoO_3) around 10% to the total amount of Mo, suggesting that they correspond to minor surface contaminations caused by potential exposure to ambient conditions. Additionally, sulfates together with moisture could form sulfites under beam exposure during the measurements.[48] The ratio between the sum of the S^{1-} and S^{2-} contribution to the Mo^{4+} species is 3.1, close to the expected MoS_3 stoichiometry. The Mo^{4+} oxidation state of MoS_3 hints at the presence of a cluster structure, as described by Weber et al.,[43] or at the chain structure model.[49] In both cases, the Mo atoms are surrounded by sulfur atoms with an oxidation state of 1-and 2-forming a local $Mo^{4+}(S^{2-})(S^{1-})_2$ structure, in good agreement with the stoichiometry derived from the XPS measurements, $Mo^{4+}(S^{2-})_{1.2}(S^{1-})_{1.9}$. The element distribution of the fabricated electrode was also mapped by energy dispersive spectroscopy (EDS), which shows that S, Mo, C, N, O, and Ni elements are all uniformly distributed around the electrode (Figure S8a, Supporting Information). Combined with the results of electron probe micro-analysis (EPMA), which show the atomic ratio of S/Mo is ~3 (Figure S8b, Supporting Information), the successful deposition of MoS_3 was further confirmed.

2.3. Electrochemical Performance of these Composite Materials in Batteries

To evaluate the electrochemical performance of these composite electrodes as the sulfur-equivalent cathodes for Li-S batteries, CR 2032 coin cells were assembled with a Li-metal anode in an Ar-filled glovebox. The electrolyte is 1 M LiTFSI in DOL/DME (1:1 by volume) with 0.1 M $LiNO_3$. The areal loading of active MoS_3 was kept at ~2 mg cm^{-2} unless otherwise noted. Figure S9a, Supporting Information shows the Nyquist plot of the 3D-MoS_3/PPy/NF cathode, which possesses a diameter of the semicircle in the high-frequency range associated with the charge-transfer resistance (R_{ct} ~ 140 Ω). Cyclic voltammetry (CV) curves and the discharge/charge properties of these cells were examined at room temperature. Several redox peaks are present in the stable CV curves of a 3D-MoS_3/PPy/NF-based cell when scanning from 1.2 ~ 3.0 V, as shown in **Figure 3a**. Since the electrochemical contributions of NF and PPy are negligible (Figure S10, Supporting Information), these redox peaks are contributed by the reversible redox process of MoS_3 for the insertion and extraction of Li ions. A possible mechanism has been proposed by previous reports, where the two peaks at 1.82 V and 1.42 V during the cathodic scan have been ascribed to the phase transformation of MoS_3 (MoS_2 and S) to Li_xMoS_2 and Li_2S, and the further conversion of Li_xMoS_2 to Mo and Li_2S, respectively. The three peaks at 1.81 V, 1.97 V, and 2.25 V during the anodic scan have been ascribed to the conversion reaction of Mo to Mo^{4+}, Mo^{4+} to Mo^{6+} and Li_2S to

© 2022 The Authors. *Energy & Environmental Materials* published by John Wiley & Sons Australia, Ltd on behalf of Zhengzhou University.

25750356, 2024, 2, Downloaded from https://onlinelibrary.wiley.com/doi/10.1002/eem2.12539 by Helmholtz-Zentrum Berlin Für, Wiley Online Library on [12/04/2024]. See the Terms and Conditions (https://onlinelibrary.wiley.com/terms-and-conditions) on Wiley Online Library for rules of use; OA articles are governed by the applicable Creative Commons License

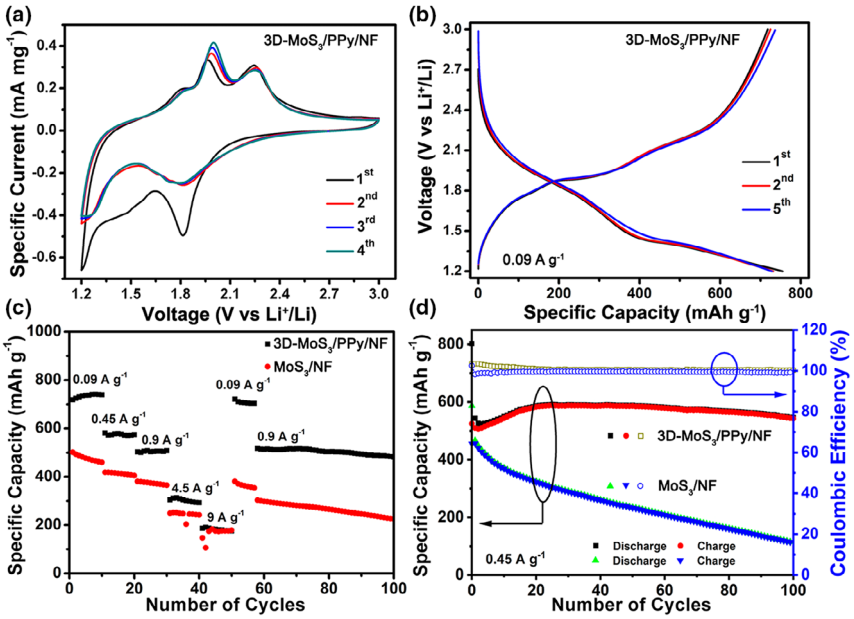


Figure 3. Electrochemical performance of 3D-MoS_3/PPy/NF and MoS_3/NF as sulfur-equivalent cathodes for Li-S batteries. a) CV curves at the scan rate of 0.1 mV s^{-1}. b) Galvanostatic charge and discharge curves at 0.09 A g^{-1}. c) Rate performance from 0.09 to 9 A g^{-1}. d) Long-term cyclic performance and Coulombic efficiency at 0.45 A g^{-1}.

S.[21,50] In this work, insights into the reaction have been performed with XANES measurements to reveal the evolution of MoS_3 as discussed later. Two sloping plateaus can be observed in the representative galvanostatic discharge/charge curves of 3D-MoS_3/PPy/NF at a current rate of 0.09 A g^{-1} between 1.2 and 3.0 V, with a stable discharge capacity reaching 730 mAh g^{-1} when normalized to the total mass of MoS_3 and 1461 mAh g^{-1} when normalized to the sulfur weight (Figure 3b). A comparison of this work with representative reported works has been summarized (Table S3, Supporting Information). Note that large variations in working conditions such as voltage range and current density can greatly affect the capacity performance. In spite of these influences, the 3D-MoS_3/PPy NWs electrode in this work delivers comparable initial capacity to the leading results of the MoS_3-based cathodes reported recently. In comparison, MoS_3/NF exhibits a lower and rapid decay of capacity, which reaches max. 500 mAh g^{-1} during the first discharge process as shown in Figure S11, Supporting Information. The superior capability of 3D-MoS_3/PPy/NF compared to the MoS_3/NF is further validated in the reversible discharge/charge capacities at various C-rates in Figure 3c. The corresponding galvanostatic charge and discharge curves of 3D-MoS_3/PPy/NF at different current densities and the following cycles at 0.9 A g^{-1} are shown in Figure S9b,c, Supporting Information. The 3D-MoS_3/PPy/NF-based cell delivers a considerable reversible capacity of ~730, 580, 503, 307, and 195 mAh g^{-1} at 0.09, 0.45, 0.9, 4.5, and 9 A g^{-1}, respectively, and back to a reversible capacity of 720 mAh g^{-1} at 0.09 A g^{-1}. The MoS_3/NF delivers an obviously lower reversible capacity of ~500 mAh g^{-1} at 0.09 A g^{-1}, 405 mAh g^{-1} (0.45 A g^{-1}), 364 mAh g^{-1} (0.9 A g^{-1}), 245 mAh g^{-1} (4.5 A g^{-1}), 193 mAh g^{-1} (9 A g^{-1}) and back to a reversible capacity of 380 mAh g^{-1} at 0.09 A g^{-1}. Conceivably, the 3D framework of PPy NWs on NF provides a larger surface for MoS_3 electrodeposition than the bare NF, which is conducive to the uniform distribution plus minimized accumulation of less conductive MoS_3, leading to a great increase of capacity compared to the MoS_3/NF-based cell with the same mass loading of MoS_3. It is notable that when increasing the loading mass of MoS_3 on PPy NWs, the capacity of 3D-MoS_3/PPy/NF also declines gradually due to the thickening of the MoS_3 layer (Figure S12, Supporting Information). This should be resulted from the decline in the conductivity of the cathode and the limited utilization of MoS_3. The diameter regulation of the PPy NWs should be an effective method to improve the performance of the 3D-MoS_3/PPy/NF with a high loading of MoS_3.

More importantly, the 3D-MoS_3/PPy/NF-based cell also exhibits good capacity retention, in which the capacity was retained at ~540 mAh g^{-1} (at 0.45 A g^{-1}) after 100 cycles with a retention of 93% (Figure 3d). Besides, the long-term cycling of the battery has been performed at 0.9 A g^{-1} for 400 cycles, which delivers an initial capacity of 450 mAh g^{-1} and a capacity retention of ~70% with a Coulombic efficiency of ~100%. In contrast, a low discharge capacity of ~112 mAh g^{-1} (at 0.45 A g^{-1}) with a rapid decline process has been maintained with the MoS_3/NF-based cell after 100 cycles.

To understand the high performance of 3D-MoS_3/PPy/NF-based batteries, these cathodes were further examined by SEM to unveil the morphology change. **Figure 4**a,b show a comparison of SEM images of 3D-MoS_3/PPy/NF electrodes before and after cycling. The framework of 3D-MoS_3/PPy remains intact but dense, with the PPy NWs thickening and forming larger particles after cycling (inset of Figure 4b). We ascribe this to the volume expansion of MoS_3 after the insertion of Li ions. This indicates the alleviation role of the PPy NWs in the volume expansion of cathode materials. For comparison, the layer of MoS_3 NPs in the MoS_3/NF electrodes becomes cracked along with the formation of bulk products after cycling (Figure 4c,d). It is conceivable that the volume expansion of rigid MoS_3 will lead to the detachment of active materials from NF, which results in the rapid deterioration of battery performance. These results indicate that the flexible 3D framework of PPy NWs can stabilize and enhance the structural integrity of cathodes by releasing strain as well as reducing the diffusion length for ions in the nanocomposite structure, which leads to the high capacity and stability of 3D-MoS_3/PPy batteries. After the cycling test, the 3D-MoS_3/PPy/NF was further examined by XRD, in which the broad MoS_3 peak centered at ~14° still can be observed, as shown in Figure S14a, Supporting Information. It is worth noting that no residual yellow electrolyte was observed on the separator during the disassembly process, as shown in Figure S14b, Supporting Information. This result indicates the absence of polysulfides in the electrolyte.

2.4. XANES Measurements

In addition to morphological changes in the electrode, the evolution of the chemical and electronic structure of Mo and S species during the charge/discharge process has been studied with XANES measurements at the S K-edge, giving insights into the mechanism of the cathode reactions. Since the formation of lithium polysulfide is one of the biggest

© 2022 The Authors. *Energy & Environmental Materials* published by John Wiley & Sons Australia, Ltd on behalf of Zhengzhou University.

25750356, 2024, 2, Downloaded from https://onlinelibrary.wiley.com/doi/10.1002/eem2.12539 by Helmholtz-Zentrum Berlin Für, Wiley Online Library on [12/04/2024]. See the Terms and Conditions (https://onlinelibrary.wiley.com/terms-and-conditions) on Wiley Online Library for rules of use; OA articles are governed by the applicable Creative Commons License

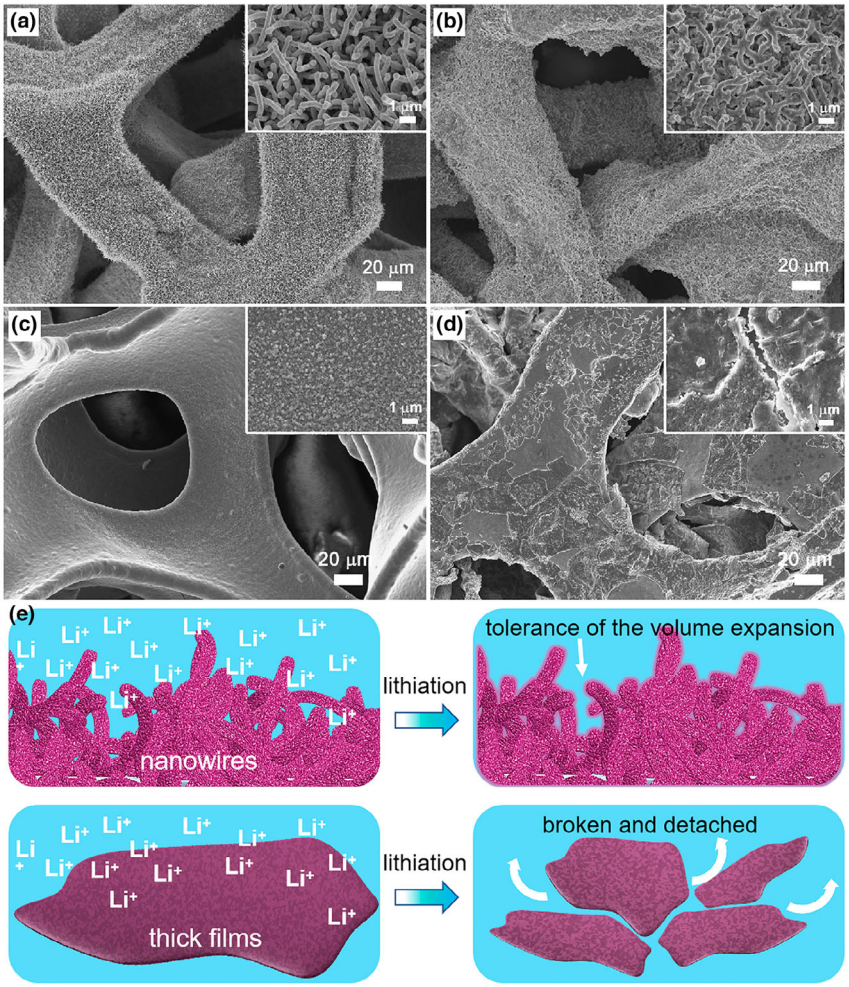


Figure 4. SEM images of the 3D-MoS_3/PPy/NF a, b) and MoS_3/NF c, d) cathodes before and after 100 charge/discharge cycles. The insets are high-magnification micrographs of the corresponding images. e) Schematic representation of the morphological change of 3D-MoS_3/PPy nanowires and MoS_3 film during lithiation.

drawbacks in current Li-S batteries, the focus of this investigation is on determining whether polysulfides are formed during discharge/charge at the 3D-MoS_3/PPy/NF cathode.

Figure 5 presents the measured S K-edge spectra of nine ex-situ prepared 3D-MoS_3/PPy/NF samples at different stages of charge (C 2.0, C 2.2, C 2.4, and C 3.0 V) and discharge (DC 1.9, DC 1.7, and DC 1.2 V). Additionally, spectra of the pristine and open circuit voltage (OCV) MoS_3 samples are presented, with the latter referring to a 3D-MoS_3/PPy/NF cathode from an uncharged electrochemical cell (after rest for ~1 week) with an OCV of 2.1 V. For a more exhaustive comparison of the MoS_3 electrodes in different (dis)charge states, Figure S15, Supporting Information shows the stacked S K-edge spectra. The DC 1.2 and C 3.0 V samples refer to the fully discharged (lithiated) and fully charged (delithiated) states, respectively. Included in Figure 5 are spectra of Li_2S_3 and Li_2S_8 reference samples from Patel et al, showing the characteristic two peak features (positions marked with black dotted lines) that all lithium polysulfides share.[51] By comparison, a formation of lithium polysulfides during the charging process seems unlikely, which is further supported by the principal component analysis of the XANES data in Figures S16–S19, Supporting Information. Hence, a formation of lithium polysulfide(s) in significant amounts (exceeding the XANES detection limit) can be excluded. These results indicate that, although the addition of PPy will sacrifice the energy density of the full batteries, the PPy NWs can supply a flexible conductive framework to construct a free-standing cathode without the additive (e.g. Super P carbon and PVDF binder). On one hand, the flexible 3D framework of PPy NWs can stabilize and enhance the structural integrity of cathodes by releasing strain as well as reducing the diffusion length for ions in the nanocomposite structure; on the other hand, this free-standing cathode can facilitate the detection of active materials for bulk-sensitive analysis (e.g. X-ray absorption near-edge spectroscopy (XANES)) by eliminating the interference from the conventional binder and carbon additive.

3. Conclusions

In summary, PPy NWs with a 3D-network structure have been fabricated for the first time on the surface of nickel foam through electrodeposition methods using a high concentration of TsOH as the soft template without the assistance of noble metals or carbon materials. The corresponding mechanism for the growth processes of PPy NWs has also been proposed. Combined with the anodic electrodeposition of MoS_3 NPs in the aqueous solution of $(NH_4)_2MoS_4$, a novel organic–inorganic MoS_3/PPy composite has been obtained and used directly to construct the sulfur-equivalent cathode of a Li-S battery. XRD and XPS measurements have been exploited to investigate the amorphous MoS_3 structure and hint at a $Mo^{4+}(S^{2-})_{1.2}(S^{1-})_{1.9}$ local structure, close to literature models with a $Mo^{4+}(S^{2-})(S^{1-})_2$ structure.[52,53] Ascribed to the flexible 3D framework of PPy NWs, the structural mechanics of cathodes are enhanced. At the same time, the active electrochemical sites increase significantly and the diffusion length for ions in the nanocomposite structure is reduced, which leads to the superior performance of 3D-MoS_3/PPy/NF-based batteries compared to the 2D-MoS_3/NF-based ones. The capacity performance of the 3D-MoS_3/PPy NWs electrode is comparable to the leading results of the MoS_3-based cathodes reported recently. Similar to recent results,[21] the formation of lithium polysulfides was excluded as the driving cathode reaction mechanism, revealing another promising property of MoS_3 as a cathode material in Li-S batteries. The results reported herein highlight a facile strategy to construct a free-standing sulfur-equivalent cathode. This strategy can not only be used in the realization of functional cathodes for, for example, Li-S batteries, but also shows great potential in the development of organic–inorganic composite materials for

© 2022 The Authors. *Energy & Environmental Materials* published by John Wiley & Sons Australia, Ltd on behalf of Zhengzhou University.

25750356, 2024, 2, Downloaded from https://onlinelibrary.wiley.com/doi/10.1002/eem2.12539 by Helmholtz-Zentrum Berlin Für, Wiley Online Library on [12/04/2024]. See the Terms and Conditions (https://onlinelibrary.wiley.com/terms-and-conditions) on Wiley Online Library for rules of use; OA articles are governed by the applicable Creative Commons License

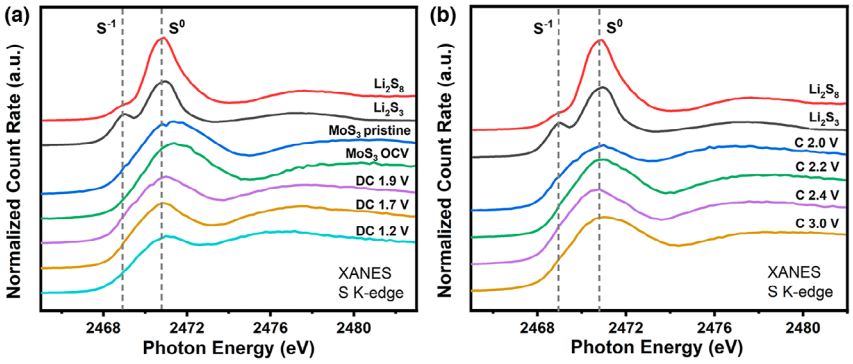


Figure 5. S K-edge spectra of the 3D-MoS_3/PPy/NF samples after a) discharge (DC) and b) charging (C) steps. Black dotted lines show the positions of features previously attributed to terminal S^{-1} and bridging S^0 peak positions of the reference lithium polysulfide spectra (as examples, Li_2S_3 and Li_2S_8 are shown here for comparison).[51]

other energy conversion and storage systems. For more practicability of this method, our further studies on the optimization of the flexible substrate and conducting polymer materials toward more light and higher conductive 3D framework electrodes are underway.

4. Experimental and Methods

Electro-polymerization of PPy NWs on NF: The commercial Ni foam (thickness: 0.5 mm) was cleaned first with acetone and soaked in 2.0 M HCl for 10 min, then washed subsequently with water and ethanol for several times, and dried in a vacuum oven at room temperature. The 3D-network PPy NWs were grown on NF by electrochemical polymerization in an aqueous solution (10 mL) containing 0.380 g Na_2HPO_4, 0.312 g NaH_2PO_4, 0.1 M p-toluenesulfonyl, and pyrrole (98%) with a different concentration. This process was conducted in a two-electrode system with a current density of 2 mA cm^{-2} for 2000 s by using an electrochemical workstation (GAMRY) and NF as the working electrode, and carbon plate as the counter and reference electrodes. After electro-polymerization, these electrodes were rinsed with H_2O several times and dried in a vacuum oven, which were then used for the modification of MoS_3. The mass of PPy NWs obtained by electronic scales was ~1.0 mg cm^{-2}. The electrode samples with different electro-polymerization time were used for the investigation of the growth mechanism of PPy NWs.

Preparation of 3D-MoS_3/PPy/NF and MoS_3/NF cathodes: The typical 3D-MoS_3/PPy/NF electrode was fabricated as follows: first, the MoS_3 NPs were deposited on the PPy NWs through anodic electrodeposition method in 50 mM $(NH_4)_2MoS_4$ aqueous solution at 0.5 V for different durations using a three-electrode system (Ag/AgCl as reference electrode and Pt wire as a counter electrode); then the obtained electrode was rinsed with water and immersed in 5 mL H_2O; 70 µL 1 M HCl was then slowly added into the solution with shaking and then immersing for 6 h. After that, the electrode was rinsed with water and dried in a vacuum oven. Finally, the electrode was annealed under Ar protection at 200 °C for 2 h. The MoS_3/NF electrodes were fabricated with the same method using NF without PPy. The mass loading of MoS_3 was obtained by weighting the masses of the electrode before and after electrodeposition of MoS_3. The areal loading of active MoS_3 was kept at ~2 mg cm^{-2} unless otherwise noted. The sulfur content by weight ratio is 22% as determined by Electron Probe MicroAnalysis (EPMA).

Materials characterization: The morphologies and structures of samples were examined by scanning electron microscopy (SEM, LEO 1530) with an EDS attachment (Zeiss). Compositional analysis was conducted using the JEOL EMPA-1600 instrument running with the accelerating voltage of 15 kV, take-off angle at 52.5°, and scanned area of 100 µm × 100 µm. The sample was analyzed three-fold on areas of the same spot. The quantitative result was obtained by the calculated mean value of the measurements. XRD (Bruker D8) was performed using a monochromatized X-ray beam with Cu Kα radiation at a scan rate of 0.05° min^{-1}. XPS (ESCALAB 250Xi; Thermo Scientific) with a monochromatized Al K_α radiation was employed to analyze the composition of the 3D-MoS_3/PPy/NF sample and the binding energy was calibrated with the C 1s spectrum, setting the adsorbed hydrocarbon peak to a binding energy of 284.8 eV. The XANES measurements on the 3D-MoS_3/PPy/NF electrode samples at different stages of discharge/charge were performed in ultra-high vacuum (UHV) with a base pressure $< 1 \times 10^{-8}$ mbar at the HiKE endstation located at the BESSY II KMC-1 beamline (beam focus size 0.1 × 0.1 mm^2) at HZB. Detailed information regarding the XPS data analysis and XANES measurements of the prepared MoS_3 samples is shown in the Appendix S1, Supporting Information.

Electrochemical measurements: The cell batteries were assembled in an Ar-filled glovebox with the concentration of moisture and oxygen <1.0 p.p.m. Coin type (CR 2032) cells were fabricated by assembling a 3D-MoS_3/PPy/NF or MoS_3/NF cathode, a Celgard 2400 diaphragm separator, and a lithium foil anode with 30 µL electrolyte. The electrolyte was prepared by dissolving 1 M Li bis(trifluoromethane)sulfonamide (LiTFSI) and 0.1 M lithium nitride ($LiNO_3$) in a mixture solution of 1,3-dioxolane and 1,2-dimethoxyethane (1:1 by volume). The galvanostatic charge/discharge tests were performed using a Biologic electrochemical workstation (MPG2 galvanostat/potentiostat) at different current densities within a cutoff voltage window of 1.2–3.0 V. The specific capacity is calculated based on the mass of MoS_3.

Acknowledgements

H.Y. and A.S. contributed equally to this work. H. T. Yu thanks the China and Germany Postdoctoral Exchange Program for this research in the Helmholtz-Zentrum Berlin für Materialien und Energie GmbH. The authors also thank the Joint Lab for Structural Research at the Integrative Research Institute for the Sciences (IRIS Adlershof). This work is supported by the National Science Foundation for Young Scientists of China (21704040). We thank HZB for the allocation of synchrotron radiation beamtime. Furthermore, the authors acknowledge the financial support of the Helmholtz Association. Open Access funding enabled and organized by Projekt DEAL.

Conflict of interest

The authors declare no conflict of interest.

Supporting Information

Supporting Information is available from the Wiley Online Library or from the author.

Keywords

3D-Network, electrochemical, lithium-sulfur battery, MoS_3, PPy

Received: June 22, 2022
Revised: September 14, 2022
Published online: September 25, 2022

© 2022 The Authors. *Energy & Environmental Materials* published by John Wiley & Sons Australia, Ltd on behalf of Zhengzhou University.

25750356, 2024, 2, Downloaded from https://onlinelibrary.wiley.com/doi/10.1002/eem2.12539 by Helmholtz-Zentrum Berlin Für, Wiley Online Library on [12/04/2024]. See the Terms and Conditions (https://onlinelibrary.wiley.com/terms-and-conditions) on Wiley Online Library for rules of use; OA articles are governed by the applicable Creative Commons License

[1] Z. W. Seh, Y. Sun, Q. Zhang, Y. Cui, *Chem. Soc. Rev.* **2016**, *45*, 5605.
[2] M. Yan, W.-P. Wang, Y.-X. Yin, L.-J. Wan, Y.-G. Guo, *Energy Chem.* **2019**, *1*, 100002.
[3] J. Yu, J. Xiao, A. Li, Z. Yang, L. Zeng, Q. Zhang, Y. Zhu, L. Guo, *Angew. Chem. Int. Ed.* **2020**, *59*, 13071.
[4] Y. Li, C. Wang, W. Wang, A. Y. S. Eng, M. Wan, L. Fu, E. Mao, G. Li, J. Tang, Z. W. Seh, *ACS Nano* **2019**, *14*, 1148–57.
[5] Y. Chen, T. Wang, H. Tian, D. Su, Q. Zhang, G. Wang, *Adv. Mater.* **2021**, *33*, 2003666.
[6] Y. Yin, S. Xin, Y. Guo, L. Wan, *Angew. Chem.* **2013**, *52*, 13186.
[7] X. Tao, J. Wang, Z. Ying, Q. Cai, G. Zheng, Y. Gan, H. Huang, Y. Xia, C. Liang, W. Zhang, *Nano Lett.* **2014**, *14*, 5288.
[8] L. Yin, J. Wang, F. Lin, J. Yang, Y. Nuli, *Energy Environ. Sci.* **2012**, *5*, 6966.
[9] R. Deng, M. Wang, H. Yu, S. Luo, J. Li, F. Chu, B. Liu, F. Wu, *Energy Environ. Mat.* **2022**, *5*, 777.
[10] M. Dekker, *Chemistry & Physics of Carbon*, Vol. *16*, Press, New York, NY **1994**.
[11] W. Li, Q. Zhang, G. Zheng, Z. W. Seh, H. Yao, Y. Cui, *Nano Lett.* **2013**, *13*, 5534.
[12] C. Tang, B. Li, Q. Zhang, L. Zhu, H. Wang, J. Shi, F. Wei, *Adv. Funct. Mater.* **2016**, *26*, 577.
[13] G. Li, J. Sun, W. Hou, S. Jiang, Y. Huang, J. Geng, *Nat. Commun.* **2016**, *7*, 10601.
[14] Y. Zhong, K. R. Yang, W. Liu, P. He, V. S. Batista, H. Wang, *J. Phys. Chem. C* **2017**, *121*, 14222.
[15] Z. W. Seh, J. H. Yu, W. Li, P. Hsu, H. Wang, Y. Sun, H. Yao, Q. Zhang, Y. Cui, *Nat. Commun.* **2014**, *5*, 5017.
[16] Z. Li, J. Zhang, X. W. D. Lou, *Angew. Chem.* **2015**, *54*, 12886.
[17] S. Hu, M. Yi, S. H. Siyal, D. Wu, H. Wang, Z. Zhu, J. Zhang, *J. Mater. Chem. A* **2021**, *9*, 15269.
[18] P. Geng, M. Du, X. Guo, H. Pang, Z. Tian, P. Braunstein, Q. Xu, *Energy Environ. Mat.* **2022**, *5*, 599.
[19] J. Ning, H. Yu, S. Mei, Y. Schütze, S. Risse, N. Kardjilov, A. Hilger, I. Manke, A. Bande, V. G. Ruiz, *Chem. Sus. Chem* **2022**, *15*, e202200434.
[20] M. Wu, Y. Cui, A. Bhargav, Y. Losovyj, A. P. Siegel, M. Agarwal, Y. Ma, Y. Fu, *Angew. Chem.* **2016**, *55*, 10027.
[21] H. Ye, L. Ma, Y. Zhou, L. Wang, N. Han, F. Zhao, J. Deng, T. Wu, Y. Li, J. Lu, *Proc. Natl. Acad. Sci. U. S. A.* **2017**, *114*, 13091.
[22] S.-R. Deng, L.-B. Kong, G.-Q. Hu, T. Wu, D. Li, Y.-H. Zhou, Z.-Y. Li, *Electrochim. Acta* **2006**, *51*, 2589–93.
[23] S. Zhang, K. Ueno, K. Dokko, M. Watanabe, *Adv. Energy Mater.* **2015**, *5*, 1500117.
[24] M. Hagen, D. Hanselmann, K. Ahlbrecht, R. Maca, D. Gerber, J. Tubke, *Adv. Energy Mater.* **2015**, *5*, 1401986.
[25] D.-Y. Wang, W. Guo, Y. Fu, *Acc. Chem. Res.* **2019**, *52*, 2290–300.
[26] H. Chen, G. Ke, X. Wu, W. Li, Y. Li, H. Mi, L. Sun, Q. Zhang, C. He, X. Ren, *Chem. Eng. J.* **2021**, *406*, 126775.
[27] S. Zeng, L. Li, L. Xie, D. Zhao, N. Wang, S. Chen, *Chemsuschem* **2017**, *10*, 3378.
[28] E. Smela, *Adv. Mater.* **2003**, *15*, 481.
[29] Z. Huang, Y. Song, X. Xu, X. Liu, *ACS Appl. Mater. Interf.* **2015**, *7*, 25506.
[30] Z. Cai, C. R. Martin, *J. Am. Chem. Soc.* **1989**, *111*, 4138.
[31] X. Zhang, S. K. Manohar, *J. Am. Chem. Soc.* **2004**, *126*, 12714.
[32] C. Debiemme-Chouvy, *Electrochem. Commun.* **2009**, *11*, 298.
[33] J. Huang, K. Wang, Z. Wei, *J. Mater. Chem.* **2010**, *20*, 1117.
[34] Z. Xia, S. Wang, Y. Li, L. Jiang, H. Sun, S. Zhu, D. S. Su, G. Sun, *J. Mater. Chem.* **2013**, *1*, 491.
[35] Z. Xia, S. Wang, L. Jiang, H. Sun, G. Sun, *J. Power Sources* **2014**, *256*, 125.
[36] X. Yang, Z. Lin, J. Zheng, Y. Huang, B. Chen, Y. Mai, X. Feng, *Nanoscale* **2016**, *8*, 8650–7.
[37] C. Debiemme-Chouvy, T. T. M. Tran, *Electrochem. Commun.* **2008**, *10*, 947.
[38] H. Kim, J. Lee, H. Ahn, O. Kim, M. J. Park, *Nat. Commun.* **2015**, DOI: 10.1038/ncomms8278.
[39] H. Yu, T. Quan, S. Mei, Z. Kochovski, W. Huang, H. Meng, Y. Lu, *Nano-micro Letters* **2019**, *11*, 41.
[40] J. Pfrommer, A. Azarpira, A. Steigert, K. Olech, P. W. Menezes, R. F. Duarte, X. Liao, R. G. Wilks, M. Bär, T. Schedel-Niedrig, *ChemCatChem* **2017**, *9*, 672.
[41] W. Zhang, T. Zhou, J. Zheng, J. Hong, Y. Pan, R. Xu, *ChemSusChem* **2015**, *8*, 1464.
[42] X.-R. Yu, F. Liu, Z.-Y. Wang, Y. Chen, *J. Electron Spectrosc. Relat. Phenom.* **1990**, *50*, 159.
[43] H. Vrubel, D. Merki, X. Hu, *Energy Environ. Sci.* **2012**, *5*, 6136.
[44] M. L. Tang, D. C. Grauer, B. Lassalle-Kaiser, V. K. Yachandra, L. Amirav, J. R. Long, J. Yano, A. P. Alivisatos, *Angew. Chem.* **2011**, *123*, 10385.
[45] T. Matsuyama, M. Deguchi, A. Hayashi, M. Tatsumisago, T. Ozaki, Y. Togawa, S. Mori, *Electrochemistry* **2015**, *83*, 889.
[46] L. Benoist, D. Gonbeau, G. Pfister-Guillouzo, E. Schmidt, G. Meunier, A. Levasseur, *Thin Solid Films* **1995**, *258*, 110.
[47] R. Jones, J. Adams, S. Evans, *Mater. Res. Bull.* **1987**, *22*, 351.
[48] S. S. Al-Shihry, S. A. Halawy, *J. Mol. Catal. A Chem.* **1996**, *113*, 479.
[49] J. Reichardt, M. Bär, A. Grimm, I. Kötschau, I. Lauermann, S. Sokoll, M. Lux-Steiner, C.-H. Fischer, C. Heske, L. Weinhardt, *Appl. Phys. Lett.* **2005**, *86*, 172102.
[50] U. Chang, J. T. Lee, J. Yun, B. Lee, S. W. Lee, H. Joh, K. Eom, T. F. Fuller, *ACS Nano* **2018**, *13*, 1490.
[51] M. U. M. Patel, I. Arcon, G. Aquilanti, L. Stievano, G. Mali, R. Dominko, *ChemPhysChem* **2014**, *15*, 894.
[52] M. E. Fleet, X. Liu, S. L. Harmer, P. L. King, *Can. Mineral.* **2005**, *43*, 1605.
[53] T. Weber, J. C. Muijsers, J. W. Niemantsverdriet, *J. Phys. Chem.* **1995**, *99*, 9194.

© 2022 The Authors. *Energy & Environmental Materials* published by John Wiley & Sons Australia, Ltd on behalf of Zhengzhou University.

25750356, 2024, 2, Downloaded from https://onlinelibrary.wiley.com/doi/10.1002/eem2.12539 by Helmholtz-Zentrum Berlin Für, Wiley Online Library on [12/04/2024]. See the Terms and Conditions (https://onlinelibrary.wiley.com/terms-and-conditions) on Wiley Online Library for rules of use; OA articles are governed by the applicable Creative Commons License